Review of Scientific Instruments

High resolution time- and angle-resolved photoemission spectroscopy with 11 eV laser pulses

Cite as: Rev. Sci. Instrum. **91**, 043102 (2020); https://doi.org/10.1063/1.5139556
Submitted: 21 November 2019 . Accepted: 18 March 2020 . Published Online: 09 April 2020

Changmin Lee, Timm Rohwer, Edbert J. Sie, Alfred Zong, Edoardo Baldini, Joshua Straquadine, Philip Walmsley, Dillon Gardner, Young S. Lee, Ian R. Fisher, and Nuh Gedik

COLLECTIONS

This paper was selected as an Editor's Pick

View Online Export Citation CrossMark

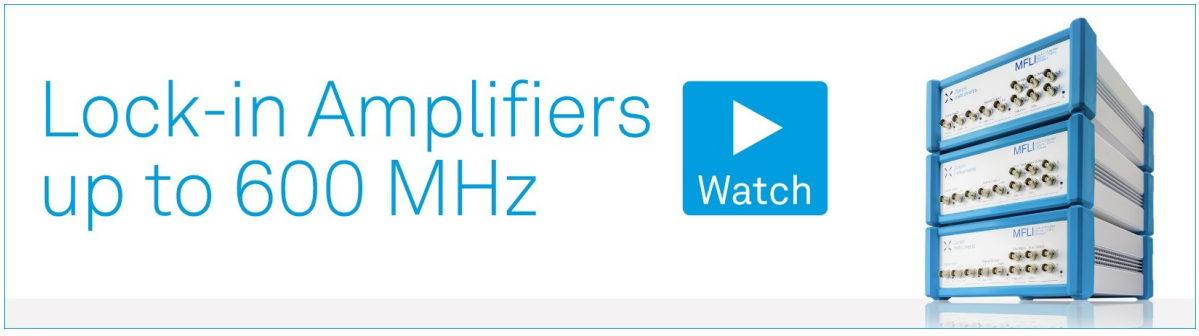

© 2020 Author(s).

Review of Scientific Instruments ARTICLE scitation.org/journal/rsi

High resolution time- and angle-resolved photoemission spectroscopy with 11 eV laser pulses

Cite as: Rev. Sci. Instrum. 91, 043102 (2020); doi: 10.1063/1.5139556
Submitted: 21 November 2019 • Accepted: 18 March 2020 •
Published Online: 9 April 2020

View Online Export Citation CrossMark

Changmin Lee,[1,a] Timm Rohwer,[1,b] Edbert J. Sie,[1,c] Alfred Zong,[1] Edoardo Baldini,[1] Joshua Straquadine,[2,3,4] Philip Walmsley,[2,3,4] Dillon Gardner,[1] Young S. Lee,[1,3,4] Ian R. Fisher,[2,3,4] and Nuh Gedik[1,d]

AFFILIATIONS

[1]Department of Physics, Massachusetts Institute of Technology, Cambridge, Massachusetts 02139, USA
[2]Geballe Laboratory for Advanced Materials, Stanford University, Stanford, California 94305, USA
[3]Department of Applied Physics, Stanford, California 94305, USA
[4]SIMES, SLAC National Accelerator Laboratory, Menlo Park, California 94025, USA

[a]**Present address:** Materials Science Division, Lawrence Berkeley National Laboratory, Berkeley, CA 94720, USA.
[b]**Present address:** Center for Free-Electron Laser Science, Deutsches Elektronen Synchrotron, 22607 Hamburg, Germany.
[c]**Present address:** Geballe Laboratory for Advanced Materials, Stanford University, Stanford, CA 94305, USA.
[d]**Author to whom correspondence should be addressed:** gedik@mit.edu

ABSTRACT

Performing time- and angle-resolved photoemission (tr-ARPES) spectroscopy at high momenta necessitates extreme ultraviolet laser pulses, which are typically produced via high harmonic generation (HHG). Despite recent advances, HHG-based setups still require large pulse energies (from hundreds of μJ to mJ) and their energy resolution is limited to tens of meV. Here, we present a novel 11 eV tr-ARPES setup that generates a flux of 5×10^{10} photons/s and achieves an unprecedented energy resolution of 16 meV. It can be operated at high repetition rates (up to 250 kHz) while using input pulse energies down to 3 μJ. We demonstrate these unique capabilities by simultaneously capturing the energy and momentum resolved dynamics in two well-separated momentum space regions of a charge density wave material $ErTe_3$. This novel setup offers the opportunity to study the non-equilibrium band structure of solids with exceptional energy and time resolutions at high repetition rates.

Published under license by AIP Publishing. https://doi.org/10.1063/1.5139556

INTRODUCTION

Angle-resolved photoemission spectroscopy (ARPES) has been at the forefront in the study of solids. Its capability of directly revealing the band structure has helped scientists to study the electronic properties of various systems ranging from metals and semiconductors to superconductors and topological materials. With the technological advance in femtosecond laser systems and nonlinear optics, time-resolved measurements of ARPES spectra in a tabletop setting are now becoming more common.[1–3] In a typical time-resolved ARPES (tr-ARPES) measurement, one laser pulse excites the system to higher energies and a subsequent ultraviolet pulse ejects the photoelectrons from the solid. Tuning the time delay between the two pulses allows the measurement of the non-equilibrium band structure, which often reveals unoccupied states in the conduction band,[4,5] the presence of collective modes such as phonons or charge density wave (CDW) amplitude modes,[6] and creation of exotic non-equilibrium electronic states[7,8] that are not present in the absence of laser pulse excitation.

As femtosecond lasers generally operate in the near-infrared regime, multiple nonlinear crystals (e.g., β-barium borate) are employed to generate ultraviolet laser pulses through frequency multiplication. With such crystals, however, output wavelengths are capped to ~190 nm (6.5 eV) due to the absorption edge and limited birefringence of the crystal.[9] While the potassium beryllium fluoroborate (KBBF) crystal allows the implementation of

Published under license by AIP Publishing

high-resolution ARPES experiments with photon energies up to 7 eV,[10–12] the momentum range covered by such light sources is still not wide enough to reach the edges or corners of the first Brillouin zone of typical solids (1 Å^{-1}). The following equation describes how much in-plane crystal momentum k can be covered with a certain photon energy $\hbar\omega$ in a photoemission experiment at the Fermi energy:

$$k = \frac{\sqrt{2mE_{\text{kin}}}}{\hbar}\sin\theta = \frac{1}{\hbar}\sqrt{2m(\hbar\omega - \varphi)}\sin\theta, \quad (1)$$

where m is the free electron mass, E_{kin} is the photoelectron kinetic energy, φ is the work function of the solid, and θ is the polar emission angle with respect to the surface normal. It is clear from Eq. (1) that higher photon energies yield larger photoelectron kinetic energies and thus a wider coverage of the momentum space.

High energy photons in the extreme ultraviolet (XUV) range are typically produced through high harmonic generation (HHG), which is a nonlinear optical process in which the frequency ω of an intense laser beam is upconverted to $n\omega$ through interaction with a medium (gas or solid, but typically inert gas). The output photon energies from HHG can range up to soft x rays.[13,14] If the inversion symmetry is present in such targets, only odd-order harmonics are produced from the HHG process. Due to the extremely nonlinear nature of HHG, large electric fields are desirable to improve the generation efficiency. This requires using high laser pulse energies and shorter pulse durations as the seed pulse for HHG. As the pulse energy and the repetition rate are inversely proportional to each other for most laser systems (at constant average power), efficient HHG sources typically operate at low repetition rates (1–10 kHz). In this case, however, ARPES spectra often suffer from poor energy resolution due to the broad bandwidth of HHG pulses and insufficient statistics as the number of electrons per pulse has to be limited in order to avoid severe space-charge effects.[15–24] Recent developments in fiber-based HHG setups, on the other hand, can suffer from lattice heating effects due to the excessively high repetition rates.[25,26] It is therefore highly desirable to produce HHG pulses at an intermediate rate (100 kHz–1 MHz) for time-resolved ARPES experiments in the weak perturbation regime.

In this work, we produce bright 11 eV laser pulses at high repetition rates (100 kHz and 250 kHz) through a series of two harmonic generation stages—a third harmonic generation (THG, Light Conversion HIRO) of 1038 nm, 190 fs Yb:KGW amplifier laser pulses (Light Conversion PHAROS) using nonlinear crystals and another THG through a hollow-core fiber (KM Labs XUUS) filled with xenon gas. Since only 3 W of the amplifier output is routed toward the harmonic generation arm, the remaining 7 W is used to pump the optical parametric amplifier (OPA, Light Conversion ORPHEUS) that generates a tunable range of wavelengths from the ultraviolet to near-infrared range. All elements of the system (OPA, DFG, and harmonic generator) are configured to be switchable between 100 kHz and 250 kHz repetition rates through minimal optical alignment procedures.

OVERVIEW OF THE SETUP

The overall scheme of the experimental setup is summarized in Fig. 1. The 3ω beam is focused onto an ~100 μm spot [full-width at

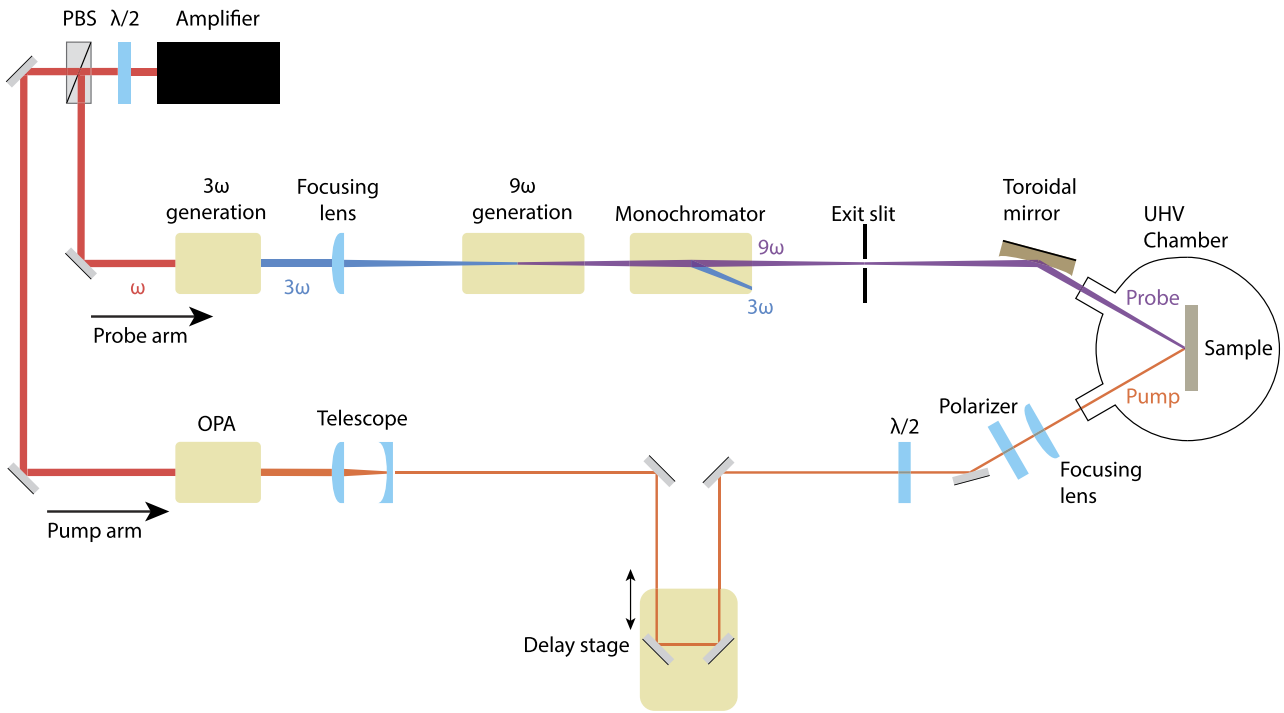

FIG. 1. The 11 eV setup. A simplified diagram of the beam paths in the 11 eV tr-ARPES setup. OPA: optical parametric amplifier and PBS: polarizing beam splitter.

Published under license by AIP Publishing

half-maximum (FWHM)] at the entrance of the hollow-core fiber filled with xenon gas in which another THG process upconverts part of the 3ω beam to 9ω. We note that the fifth harmonic generation of 3ω is extremely weak in the current configuration, indicating that the harmonic generation is highly perturbative. This process is clearly distinct from HHG in which the flux of the generated harmonics is similar in size over a wide range of harmonic orders ("plateau region").[13,14] A set of waveplate and polarizer are also placed before the fiber to control the input power. Both the 3ω and 9ω beams co-propagate into the monochromator, which is directly connected to the hollow-core fiber under vacuum.

The monochromator mainly serves to filter out 3ω and transmits 9ω to the ARPES chamber. The off-plane Czerny–Turner monochromator was custom-built from McPherson Inc. (model: OP-XCT), and its design was inspired by the single-grating monochromator reported in Ref. 27. A more detailed description of the monochromator is also provided in Ref. 28. The gold-coated grating has 500 grooves per mm (Richardson gratings), and it is mounted in an "off-plane" geometry so that the rulings are oriented parallel to the propagation direction of the beam. Under such geometry, the following equation satisfies the diffraction condition:[29]

$$2 \sin \psi \sin \Lambda = n\lambda\sigma, \tag{2}$$

where ψ is the azimuthal angle of the grating, Λ is the incidence angle of the beam with respect to the groove direction, n is the diffraction order, λ is the wavelength of the diffracted beam, and σ is the groove density. The 9ω (11 eV) beam travels at ~5° with respect to the grating, and a sharp diffraction peak is observed when ψ is set to ~20°.

The output of the monochromator is terminated with a 0.5 mm thick LiF window (Korth Kristalle GmbH) mounted on an ultra-high vacuum (UHV) gate valve (VAT Inc.). During measurements, we use the LiF window to stop the inert gas flow into the UHV ARPES chamber. The LiF window is much more robust compared to thin metallic windows used in typical HHG experiments, providing an ease of operation during the alignment procedures and a complete separation of the harmonic generation pressure from the final ARPES chamber under UHV. There is negligible group velocity dispersion at 11 eV for 150–200 fs pulses we use through a 0.5 mm LiF window. This only becomes relevant for pulses shorter than 50 fs. The typical transmission of 11 eV through the LiF window was measured to be ~20%–30%. As the LiF window also transmits the 3ω (3.6 eV) beam, the monochromator grating plays a crucial role in ensuring that only the 9ω (10.8 eV) component is transmitted to the ARPES chamber. The 11 eV output beam then focuses at the exit slits of the monochromator. The slit openings can be tuned to control the spot size at the sample, as the exit slit is imaged to the sample in a 1:1 configuration.

The 11 eV beam then travels into the multi-port diagnostic chamber (Kimball Physics) in which the beam profile and intensity can be monitored. A toroidal gold-coated mirror can be inserted into the chamber to direct the 11 eV beam toward the CCD (Andor Newton) in which the overall intensity and fiber propagation mode of the 11 eV beam can be diagnosed from the CCD images. When the toroidal mirror is retracted from the beam path, the 11 eV flux can be measured more accurately with a photodiode (AXUV 100 G, Opto Diode Corp.) by means of lock-in detection (Table I).

TABLE I. 11 eV output intensity measured at the diagnostic chamber (before the final focusing toroidal mirror).

Repetition rate (kHz)	Input 3ω pulse energy (μJ)	Photons/s
100	7	4.7×10^{10}
250	3	2.4×10^{10}

We find that the 11 eV generation efficiency is higher at the 100 kHz repetition rate under the same input power (pulse energy, on the other hand, is 2.5 times larger). The 11 eV beam then reflects off of a fixed toroidal mirror and focuses onto the sample mounted inside the ARPES chamber in which the pressure is maintained at $<1 \times 10^{-10}$ Torr.

Bi_2Se_3 MEASUREMENTS—TIME AND ENERGY RESOLUTIONS

Assuming that various contributions to the broadening of spectra (bandwidth of 11 eV, analyzer resolution, etc.,) can be collectively modeled with a Gaussian profile, the energy distribution curve (EDC) across the Fermi edge can be fitted using a Gaussian-convoluted Fermi–Dirac distribution,

$$\begin{aligned} I(E) &= [f(E,T)D(E)] \otimes g(E) \\ &= \frac{D(E)}{e^{(E-E_F)/k_BT}+1} \otimes e^{-4\ln 2\, E^2/\mathrm{FWHM}_E^2}, \end{aligned} \tag{3}$$

where $D(E)$ is the density of states, $E - E_F$ is the photoelectron energy with respect to the Fermi level, k_B is the Boltzmann constant, T is the sample temperature, and FWHM_E is the energy resolution.

In order to evaluate the performance of our instrument, we acquired ARPES spectra close to the Fermi energy of an n-doped Bi_2Se_3 single crystal. The Bi_2Se_3 sample was cleaved at 35 K under a base pressure of 1.0×10^{-10} Torr. The time-of-flight (ARTOF 10K from Scienta Omicron) detector was configured with a ±15° emission angle range and a 10% energy window under a double-pass mode. The repetition rate of the laser was set to 250 kHz. The Dirac cone surface states are clearly visible in Figs. 2(a) and 2(b) in which cuts were taken along the orthogonal in-plane directions (k_x and k_y). The Fermi energy is located 350–400 meV above the Dirac point, and signatures of the bulk conduction band can be observed close to the upper right region of the Dirac cone in Fig. 2(a). By fitting the momentum-integrated EDC data to Eq. (3), we obtain an energy resolution of 16 meV [Fig. 2(c)].

Since this monochromator was previously shown to improve the energy resolution of the ARPES setup based on HHG sources,[28,30,31] it is important to establish whether the monochromator can cut down the bandwidth of 11 eV any further. We thus measure the energy resolution of ARPES spectra taken at various slit openings [Fig. 3(a)]. As shown in Fig. 3(b), there is only a slight improvement in the resolution at smaller slit openings. The poor energy resolution at the widest slit opening possibly originates from the instrument limitation, as opposed to the broader bandwidth of

Published under license by AIP Publishing

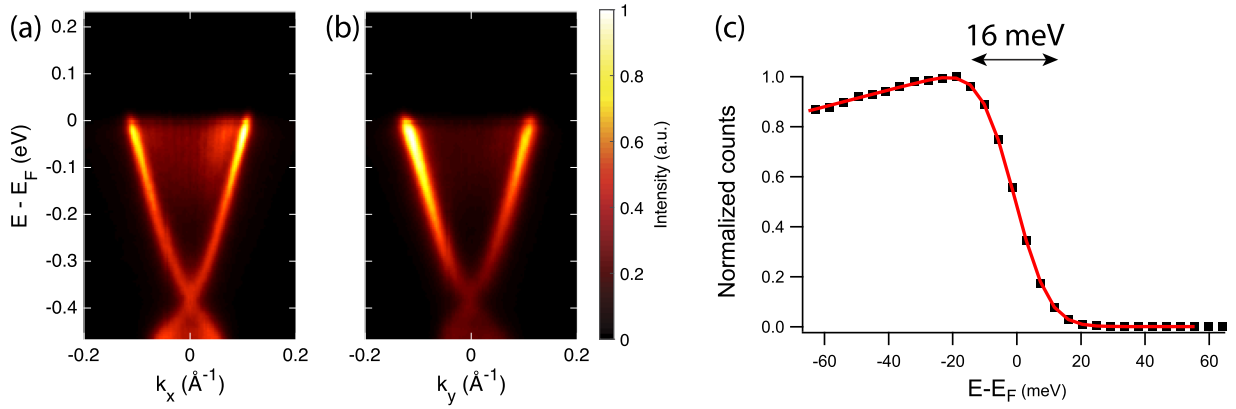

FIG. 2. ARPES spectra from Bi_2Se_3 single crystals. The linearly dispersing surface states are clearly visible in cuts along the (a) k_x and (b) k_y directions. (c) A momentum integrated (across ± 0.2 Å^{-1} along both k_x and k_y directions) EDC yields a 16 meV energy resolution. Data acquisition time was 1 h.

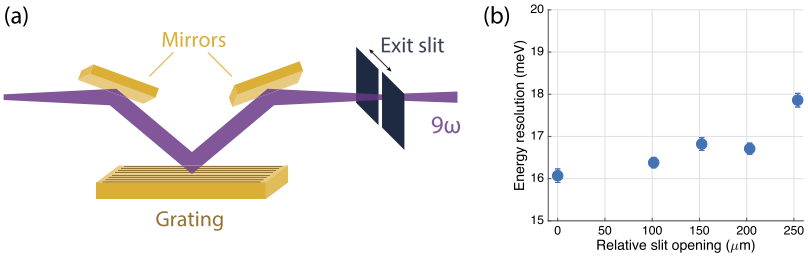

FIG. 3. Slit dependence of the energy resolution. (a) A schematic showing the beam path through the grating and the exit slit. ARPES spectra were taken at various horizontal slit opening values. (b) Energy resolution remains almost unchanged at different slit settings. Error bars represent the uncertainties of least squares fitting of momentum-integrated (across ± 0.2 Å^{-1}) EDC data to Eq. (3).

the 11 eV source. This is because the calibrations of our time-of-flight electron analyzer are optimized for spot sizes of ~100 μm. Larger focal spot sizes generally increase the uncertainties of the measured emission angle and eventually broaden the measurements of photoelectron kinetic energies.

We now turn to time-resolved measurements of the setup. We choose 680 nm (1.82 eV, incident fluence: 400 μJ/cm^2) laser pulses from the OPA to pump the system to an excited state. The angular range was set to $\pm 15^\circ$, and the energy window was set to 20% under a double-pass mode. The ARPES spectra are then taken at various time delays between the pump and probe pulses. The energy-momentum cuts in Fig. 4 show that the upper region of the Dirac cone is populated at positive time delays after photoexcitation. The wide momentum coverage is apparent from the second panel in which the photoexcited charge carriers populate >0.7 eV above the Fermi level. While a 6 eV probe beam covers ~± 0.19 A^{-1} with $\pm 15^\circ$

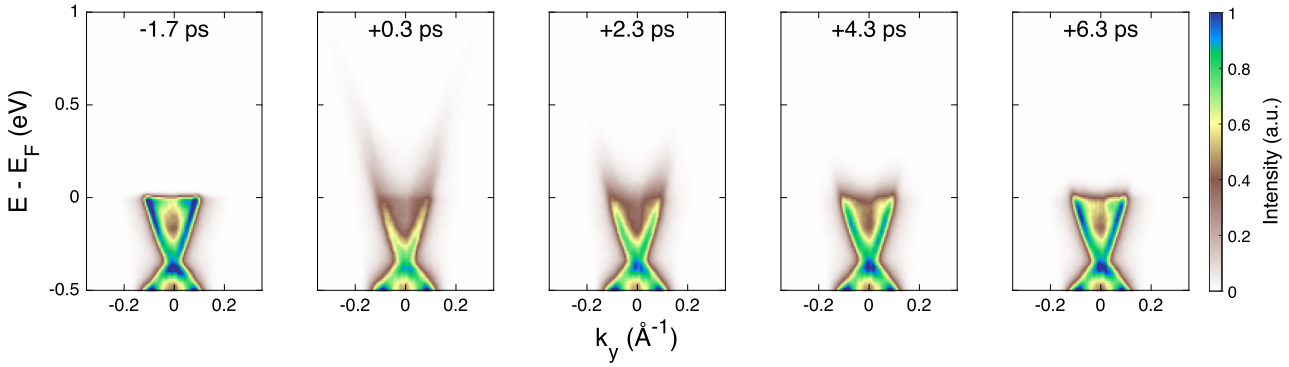

FIG. 4. Snapshots of Bi_2Se_3 tr-ARPES spectra. Energy-momentum cuts were taken across the Γ point at different time delays (displayed in the upper part of each panel) between the pump and probe pulses. The upper part of the Dirac cone is transiently populated due to photoexcitation by the 1.82 eV pump pulse. Data acquisition time for each snapshot was 15 min.

Published under license by AIP Publishing

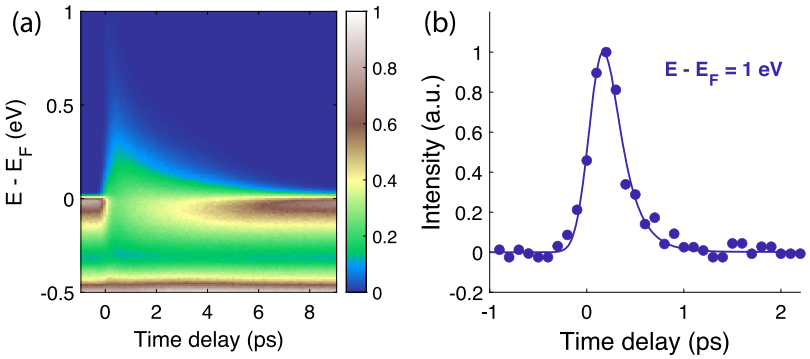

FIG. 5. Momentum-integrated, time-resolved photoemission traces of Bi_2Se_3. (a) A two-dimensional plot of the momentum-integrated photoemission (counts at different time delays and energies with respect to the Fermi level). (b) A plot of photoemission counts as a function of time delay at $E - E_F = 1$ eV, with an integration window of 10 meV. Raw data (filled circles) and fits (curves) to Eq. (4) are in good agreement. Data acquisition time was 4 h.

angular range of the detector, our 11 eV setup can measure up to ± 0.36 A^{-1}, which is almost four times as large as the momentum range of 6 eV measurements. The photoexcited charge carriers in Bi_2Se_3 gradually relax back to its equilibrium after a few picoseconds.

In order to characterize the time resolution of the setup, we plot the momentum-integrated photoelectron counts as a function of time delay at various energies above the Fermi level. The resulting contour [Fig. 5(a)] indicates that the relaxation dynamics of the photoexcited charge carriers is faster for higher energies, typical of a metallic surface. The pump–probe traces at $E - E_F = 1$ eV are then plotted by integrating the (momentum-integrated) photoemission counts over an energy window of 50 meV [Fig. 5(b)]. These time-dependent photoemission counts can be fitted with a single exponential function convolved with a Gaussian function that takes the finite experimental time resolution into the account,

$$I(t) = \left[\mathrm{Ae}^{-\frac{t-t_0}{\tau}} \cdot H(t-t_0)\right] \otimes e^{-4\ln 2\, t^2/\mathrm{FWHM}_t^2}, \tag{4}$$

where $t - t_0$ is the pump–probe time delay, τ is the relaxation time of the pump–probe signal, $H(t - t_0)$ is the Heaviside step function, and FWHM_t is the time resolution. The nonlinear least square fits of the data at $E - E_F = 1$ eV yield a FWHM resolution of 250 fs. The lower time resolution compared to the pulse width of the laser output (190 fs) probably originates from the dispersive optical elements along the pump path, finite rise time of the time-resolved spectra, and a slightly non-collinear (~10°) propagation of the pump and probe beams.

$ErTe_3$ MEASUREMENTS–RECOVERY DYNAMICS OF TWO CDW REGIONS

To further demonstrate the capability of the 11 eV setup, we present the tr-ARPES spectra of a rare-earth tri-chalcogenide system $ErTe_3$. The family of RTe_3 compounds (R = rare earth element) forms a layered orthorhombic crystal structure and typically exhibits charge density wave (CDW) gaps across a large region of the Fermi surface.[32] Prior tr-ARPES measurements on $TbTe_3$ identified amplitude modes[6] and demonstrated that the CDW state may be transiently stabilized upon near-infrared excitation.[33] A previous work using this 11 eV setup also identified a photoinduced CDW phase transition whose recovery dynamics is mediated through topological defects.[34]

Among the RTe_3 compounds, the heavier $ErTe_3$ exhibits two separate CDW phase transitions (at 155 K and 267 K) with ordering wavevectors oriented along the two orthogonal in-plane directions [see Fig. 6(a)].[35,36] The dual-CDW compound $ErTe_3$ provides an ideal platform to use the 11 eV system, as the momentum coverage is sufficiently wide to cover both CDW regions simultaneously.

Single crystals of $ErTe_3$ grown by slow cooling a binary melt[35] are air sensitive. Therefore, all procedures of sample preparation are carried out in a glovebox before the sample is mounted on the ARPES chamber. After minimal exposure to ambient pressure, the samples were cleaved *in situ* under a base pressure of 1×10^{-10} Torr at 15 K ($< T_{\mathrm{CDW1}}$ and T_{CDW2}). All measurements were taken at 100 kHz. Figure 6(a) shows a constant energy contour at the Fermi level in which a large fraction of the $ErTe_3$ Fermi surface is gapped out due to the CDW formation. By taking energy-momentum cuts [Figs. 6(c) and 6(d)] across the gapped regions [green horizontal dashed lines in Fig. 6(a)], the leading edge of the valence band yields the CDW gap sizes of ~250 meV (CDW_1) and ~50 meV (CDW_2), which are consistent with another ARPES measurement.[36] The distinct separation between the two CDW regions is apparent in Fig. 6(b), which shows a cut taken along the vertical blue dashed line shown in Fig. 6(a).

We then performed time-resolved measurements using 720 nm (1.72 eV, incident fluence: 700 μJ/cm^2) pump pulses whose photon energy exceeds the size of both CDW gaps. The snapshots of energy momentum cuts (Fig. 7, Multimedia view) reveal that the CDW gaps are transiently filled right after photoexcitation, similar to the observations reported in Refs. 6 and 33, suggesting a transient suppression of the CDW orders and a photoinduced phase transition to the normal state. The extent of gap filling is maximized at ~250 fs after the arrival of the pump pulse, indicating that ultrafast photoexcitation across the gap [Figs. 7(a) and 7(b)] precedes the photoinduced phase transition. Within 2 ps, however, the population of photoexcited carriers above the Fermi level and within the gap almost completely vanishes, and the electronic structure recovers to a quasi-equilibrium state. A key strength of our setup is the ability to simultaneously monitor the dynamics of two CDW orders within a single measurement. A close look at the relaxation dynamics within the gap reveals that the recovery is much slower for the case of CDW_2 (relaxation times: $\tau_1 = 0.60 \pm 0.08$ ps and $\tau_2 = 2.4 \pm 0.3$ ps) whose gap size is significantly smaller. This

Published under license by AIP Publishing

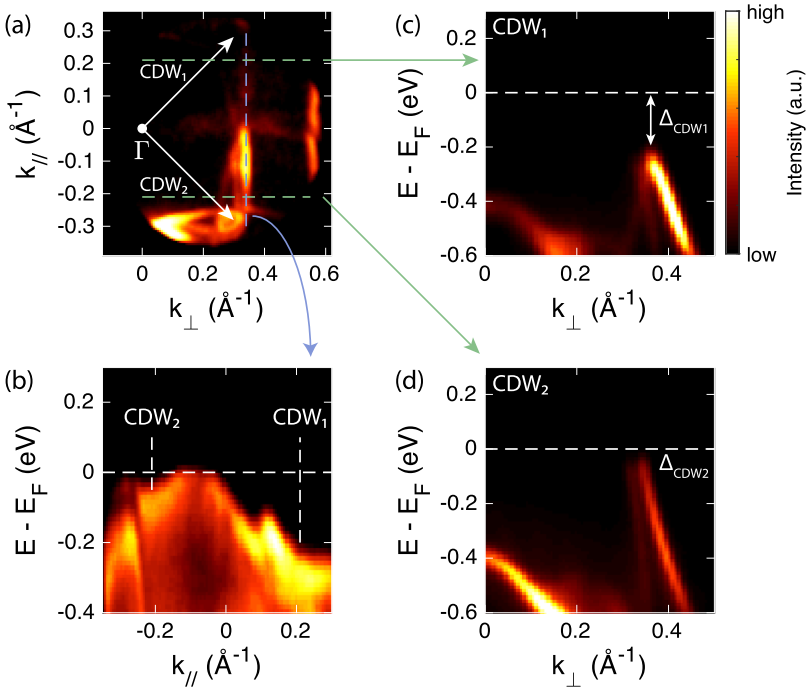

FIG. 6. Static ARPES spectra of $ErTe_3$. (a) The Fermi surface (integrated over 50 meV) exhibits a large gapped area due to the CDW formations. Energy momentum cuts were taken across the (b) vertical (blue) and [(c) and (d)] horizontal (green) lines displayed in (a) with an integration window of 0.02 $Å^{-1}$. Two distinct regions of CDW gaps are clearly observable. The momenta $k_{//}$ and $k_{\perp}$ are oriented at 45° with respect to the crystallographic axes *a* and *c* along the basal plane. Data acquisition time was 1 h.

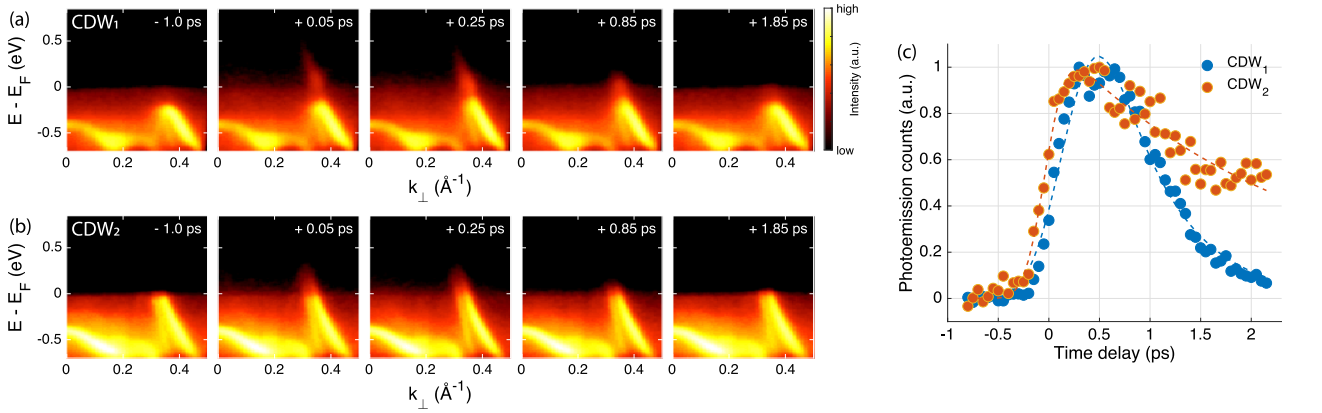

FIG. 7. tr-ARPES snapshots of $ErTe_3$. Energy momentum cuts are taken across the (a) CDW_1 and (b) CDW_2 gaps [green dashed lines shown in Fig. 6(a)] at different pump and probe time delays. The CDW gap closings are observed 0.25 ps after the arrival of the pump pulse. (c) The two CDW regions show different relaxation timescales upon pump excitation. The photoemission counts were integrated across momentum and energy ranges of ±0.05 $Å^{-1}$ and ±25 meV, respectively, around the gapped regions. The resulting data (dots) were then fitted (dashed curves) to Eq. (4) in order to extract the relaxation times. The data acquisition times were 1 h for each snapshot and 8 h for the time-resolved data. Multimedia view: https://doi.org/10.1063/1.5139556.1

observation indicates that the ordered bound-state electrons under the larger gap (Δ_{CDW1}) have a stronger tendency to form a CDW, and consequently, the relaxation is much faster than in the case of the smaller gap (Δ_{CDW2}). Another possibility is a larger phase space available for the charge carriers relaxing across Δ_{CDW1}, leading to a faster recovery time. The detailed physical mechanism leading to different dynamics in the two gaps will be presented elsewhere.

DISCUSSION

The wide momentum coverage of 11 eV combined with the 3D mapping capability of the time-of-flight electron analyzer provides a powerful method of studying the nonequilibrium band structure on sub-picosecond timescales. The tunable, fast repetition rates (100/250 kHz) of the system allows high acquisition rates as the photoelectron pulses undergo less space-charge repulsions.

Published under license by AIP Publishing

The tunability of pump photon energies also allows the system to be photoexcited under various resonance/off-resonance conditions with minimal adjustments. Above all, the unprecedented energy and time resolutions of 16 meV and 250 fs with XUV pulses enable high-resolution, momentum-selective non-equilibrium studies of the band structure across a wide range of the Brillouin zone.

Note added in proof. During the preparation of this manuscript, we became aware of two related works in which the authors use the second harmonic of a YB:KGW amplifier output as the seed pulse.[37,38] We note that the pulse energies used in these setups are significantly higher (>70 μJ) than those used in this work (3–7 μJ).

AUTHOR'S CONTRIBUTIONS

C.L., T.R., and E.J.S. contributed equally to this work.

ACKNOWLEDGMENTS

We would like to thank Ya-Qing Bie and Pablo Jarillo-Herrero for their assistance with the $ErTe_3$ sample preparation using the glovebox and Fahad Mahmood for useful discussions during the early stage of this work. E.B. acknowledges support from the Swiss National Science Foundation under fellowships P2ELP2_172290 and P400P2_183842. This work was supported by the U.S. Department of Energy, BES DMSE (Grant No. DE-FG02-08ER46521) (planning, instrumentation, and data taking), Army Research Office (Grant No. W911NF-15-1-0128, partial support for the time of flight detector and monochromator) and by the Gordon and Betty Moore Foundation's EPiQS Initiative (Grant No. GBMF4540) (support for the laser). Crystal growth and characterization of the $ErTe_3$ samples were performed at Stanford University with support from the Department of Energy, Office of Basic Energy Sciences under Contract No. DE-AC02-76SF00515.

REFERENCES

[1] L. Perfetti, P. A. Loukakos, M. Lisowski, U. Bovensiepen, H. Eisaki, and M. Wolf, Phys. Rev. Lett. **99**(19), 197001 (2007).
[2] J. Faure, J. Mauchain, E. Papalazarou, W. Yan, J. Pinon, M. Marsi, and L. Perfetti, Rev. Sci. Instrum. **83**(4), 043109 (2012).
[3] Y. Ishida, T. Togashi, K. Yamamoto, M. Tanaka, T. Kiss, T. Otsu, Y. Kobayashi, and S. Shin, Rev. Sci. Instrum. **85**(12), 123904 (2014).
[4] C. L. Smallwood, J. P. Hinton, C. Jozwiak, W. Zhang, J. D. Koralek, H. Eisaki, D.-H. Lee, J. Orenstein, and A. Lanzara, Science **336**(6085), 1137–1139 (2012).
[5] J. A. Sobota, S. Yang, J. G. Analytis, Y. L. Chen, I. R. Fisher, P. S. Kirchmann, and Z. X. Shen, Phys. Rev. Lett. **108**(11), 117403 (2012).
[6] F. Schmitt *et al.*, Science **321**(5896), 1649–1652 (2008).
[7] Y. H. Wang, H. Steinberg, P. Jarillo-Herrero, and N. Gedik, Science **342**(6157), 453–457 (2013).
[8] F. Mahmood, C.-K. Chan, Z. Alpichshev, D. Gardner, Y. Lee, P. A. Lee, and N. Gedik, Nat. Phys. **12**, 306 (2016).
[9] C. Chen, Z. Lin, and Z. Wang, Appl. Phys. B **80**(1), 1–25 (2005).
[10] T. Kiss, T. Shimojima, K. Ishizaka, A. Chainani, T. Togashi, T. Kanai, X.-Y. Wang, C.-T. Chen, S. Watanabe, and S. Shin, Rev. Sci. Instrum. **79**(2), 023106 (2008).
[11] C. Chen, Opt. Mater. **26**(4), 425–429 (2004).
[12] Z. Yong *et al.*, Chin. Phys. Lett. **25**(3), 963–965 (2008).
[13] T. Pfeifer, C. Spielmann, and G. Gerber, Rep. Prog. Phys. **69**(2), 443–505 (2006).
[14] C. Winterfeldt, C. Spielmann, and G. Gerber, Rev. Mod. Phys. **80**(1), 117–140 (2008).
[15] J. C. Petersen *et al.*, Phys. Rev. Lett. **107**(17), 177402 (2011).
[16] T. Rohwer *et al.*, Nature **471**, 490 (2011).
[17] K. Ishizaka *et al.*, Phys. Rev. B **83**(8), 081104 (2011).
[18] B. Frietsch, R. Carley, K. Döbrich, C. Gahl, M. Teichmann, O. Schwarzkopf, P. Wernet, and M. Weinelt, Rev. Sci. Instrum. **84**(7), 075106 (2013).
[19] S. Eich *et al.*, J. Electron Spectrosc. Relat. Phenom. **195**, 231–236 (2014).
[20] H. Wang, Y. Xu, S. Ulonska, J. S. Robinson, P. Ranitovic, and R. A. Kaindl, Nat. Commun. **6**, 7459 (2015).
[21] G. Rohde, A. Hendel, A. Stange, K. Hanff, L.-P. Oloff, L. X. Yang, K. Rossnagel, and M. Bauer, Rev. Sci. Instrum. **87**(10), 103102 (2016).
[22] F. Cilento, A. Crepaldi, G. Manzoni, A. Sterzi, M. Zacchigna, P. Bugnon, H. Berger, and F. Parmigiani, J. Electron Spectrosc. Relat. Phenom. **207**, 7–13 (2016).
[23] J. H. Buss *et al.*, Rev. Sci. Instrum. **90**(2), 023105 (2019).
[24] M. Puppin *et al.*, Rev. Sci. Instrum. **90**(2), 023104 (2019).
[25] A. K. Mills *et al.*, Rev. Sci. Instrum. **90**(8), 083001 (2019).
[26] C. Corder, P. Zhao, J. Bakalis, X. Li, M. D. Kershis, A. R. Muraca, M. G. White, and T. K. Allison, Struct. Dyn. **5**(5), 054301 (2018).
[27] F. Frassetto, C. Cacho, C. A. Froud, I. C. E. Turcu, P. Villoresi, W. A. Bryan, E. Springate, and L. Poletto, Opt. Express **19**(20), 19169–19181 (2011).
[28] E. J. Sie, T. Rohwer, C. Lee, and N. Gedik, Nat. Commun. **10**(1), 3535 (2019).
[29] W. Werner and H. Visser, Appl. Opt. **20**(3), 487–492 (1981).
[30] E. J. Sie, "Coherent light-matter interactions in monolayer transition-metal dichalcogenides," Ph.D. thesis, MIT, 2017.
[31] C. Lee, "Nonlinear optical and photoemission spectroscopies of quantum materials," Ph.D. thesis, MIT, 2018.
[32] V. Brouet *et al.*, Phys. Rev. B **77**(23), 235104 (2008).
[33] L. Rettig, R. Cortés, J. H. Chu, I. R. Fisher, F. Schmitt, R. G. Moore, Z. X. Shen, P. S. Kirchmann, M. Wolf, and U. Bovensiepen, Nat. Commun. **7**, 10459 (2016).
[34] A. Zong *et al.*, Nat. Phys. **15**(1), 27–31 (2019).
[35] N. Ru, C. L. Condron, G. Y. Margulis, K. Y. Shin, J. Laverock, S. B. Dugdale, M. F. Toney, and I. R. Fisher, Phys. Rev. B **77**(3), 035114 (2008).
[36] R. G. Moore, V. Brouet, R. He, D. H. Lu, N. Ru, J. H. Chu, I. R. Fisher, and Z. X. Shen, Phys. Rev. B **81**(7), 073102 (2010).
[37] Y. Liu *et al.*, Rev. Sci. Instrum. **91**, 013102 (2020).
[38] R. Cucini *et al.*, Struct. Dyn. **7**, 014303 (2020).

Published under license by AIP Publishing